Catalysis Science & Technology

ROYAL SOCIETY OF CHEMISTRY

PAPER

View Article Online
View Journal | View Issue



Cite this: *Catal. Sci. Technol.*, 2021, 11, 319

# Dual-function surface hydrogen bonds enable robust $O_2$ activation for deep photocatalytic toluene oxidation†

Hao Li,[ab] Fuze Jiang,[ab] Sarka Drdova,[ab] Huan Shang,[c] Lizhi Zhang [c] and Jing Wang *[ab]

Solar-driven molecular oxygen activation by semiconductor photocatalysts is a prototypical reaction manifesting complex interactions among photons, charge carriers, and reactants. In this study, we demonstrate that energetic $O_2$ activation towards volatile organic compound control can be realized *via* constructing a sophisticated surface hydrogen bond (HB) network having a dual-function. The extensive HBs established between the hydroxyl-rich BiOCl surface and phosphoric acid are first shown to significantly weaken surface Bi–O bonds, enabling facile oxygen vacancy (OV) generation. OVs, which act as reliable electron capture and static $O_2$ activation centers, reinforce the interaction between photons and excitons for rapid charge carrier separation. Moreover, dynamic $O_2$ activation with sluggish kinetics can be surmounted by another type of HB localized between hydroxyl groups of phosphoric acid and OV-adsorbed $O_2$. These unique localized HBs facilitate interfacial electron transfer from BiOCl to $O_2$, displaying a unique energy coupling route between charge carriers and reactants. For simulated indoor toluene oxidation, the substantially boosted $O_2$ activation is shown to accelerate the kinetic processes associated with the primary oxidation of toluene into benzaldehyde and benzoic acid, as well as aromatic ring opening towards deep oxidation. Undesirable intermediate accumulation and catalyst deactivation are thus avoided. The present work highlights the pivotal roles of HBs in robust photocatalytic $O_2$ activation. It will provide novel insights into the design of high-performance catalysts for efficient and safe control of indoor volatile organic compounds.

Received 29th September 2020,
Accepted 29th October 2020

DOI: 10.1039/d0cy01907k

rsc.li/catalysis



## Introduction

Air pollution is a critical environmental problem both now and in the coming decades. Recently, the issue of indoor air quality has received increasing attention for improving the comfort and health of building occupants.[1,2] This is because many people spend approximately 80% of their time indoors, where the concentrations of some pollutants are often 2 to 5 times greater than those in outdoor environments. Among various indoor pollutants, volatile organic compounds (VOCs) are a group of typical organic matter with adverse effects on human health, causing chronic respiratory and/or cardiovascular diseases. The mainstream technology to remove indoor VOCs is adsorption through a functional filter containing zeolite or activated carbon.[3,4] However, whether adsorption technology, which merely transfers VOCs from the gaseous phase to solid phase, is genuinely reliable for indoor air control remains questionable. For instance, adsorption is not suitable for VOCs at low concentrations (ppb and sub-ppm levels). The equilibrium adsorption capacity of functional filters is adversely affected by increased relative humidity,[5] and long-term VOC exposure increases the risk of VOC desorption and impedes the regeneration of filters. A more encouraging way to remove indoor VOCs is through deep catalytic oxidation. Ideally, VOCs can be oxidized entirely into low-risk $CO_2$ and $H_2O$. Although thermocatalytic oxidations seem promising for VOC removal, the use of noble metals as catalysts and the addition of electrically-powered heating elements will increase the cost of air purification systems. In this context, the development of energy-efficient systems with superiority in indoor VOC deep oxidation has been a goal of worldwide researchers.

The past few decades have witnessed tremendous efforts in exploring cheap metal oxides for renewable energy generation through photocatalytic water splitting, $CO_2$

[a] *Institute of Environmental Engineering, ETH Zürich, Zürich 8093, Switzerland. E-mail: jing.wang@ifu.baug.ethz.ch*
[b] *Laboratory for Advanced Analytical Technologies, Empa, Swiss Federal Laboratories for Materials Science and Technology, Dübendorf 8600, Switzerland*
[c] *Key Laboratory of Pesticide & Chemical Biology of Ministry of Education, Institute of Applied & Environmental Chemistry, College of Chemistry, Central China Normal University, Wuhan 430079, P. R. China*

† Electronic supplementary information (ESI) available. See DOI: 10.1039/d0cy01907k

reduction and $N_2$ fixation.[6–9] Besides these applications, photocatalysis has also received considerable attention for indoor VOC removal under ambient conditions. Such novel technology is environmentally benign as atmospheric oxygen ($O_2$) is harvested as a green and clean oxidant through molecular activation. It is widely accepted that oxidation capacity of $O_2$ under ambient conditions is severely hampered by spin forbidden reactions, while its activated forms ($^{\bullet}O_2^-$, $O_2^{2-}$, $H_2O_2$, or $^{\bullet}OH$) are highly active in triggering indoor VOC oxidations.[10–13] Unfortunately, room-temperature photocatalytic VOC oxidation, particularly for those aromatic compounds, is not efficient enough with a tandem bottleneck associated with risky intermediate emission and catalyst deactivation.[11,12] Toluene is a representative of aromatic VOCs whose oxidation is shown to be difficult and intricate. Rather than being directly mineralized, toluene is usually decomposed stepwise through which undesirable carbonaceous intermediates are generated *in situ*. These as-formed intermediates can be either more toxic than the parent VOCs or show strong complexation with the photocatalyst surface, thus causing secondary pollution or photocatalyst deactivation.[14–16] It cannot be emphasized enough that the formation of unfavorable carbonaceous intermediates is directly caused by the sluggish aromatic ring-opening process, which is the prerequisite step for overall toluene oxidation and an essential prerequisite for deep oxidation.[12,17] Sluggishness of aromatic ring cleavage is a "diagnostic" sign of the partial or incomplete oxidation of organics due to insufficient supply of reactive oxygen species (ROSs). In this regard, developing novel photocatalysts with strong $O_2$ adsorption and activation capability is key to deeply oxidizing aromatic VOCs.

It is widely accepted that the efficiency of photocatalytic $O_2$ activation highly relies on the interaction between photons and charge carriers. For example, carrier-based $O_2$ activation ($O_2 \rightarrow {}^{\bullet}O_2^-/O_2^{2-}$) is initiated by charge carrier generation upon photon absorption, and largely impeded by competitive resonance charge transfer or nonradiative depopulation arising from exciton–exciton annihilation.[18,19] To accelerate charge carrier separation, Xie and co-workers proposed the introduction of oxygen vacancies (OVs) into photocatalysts by strengthening photon–exciton coupling.[20,21] Moreover, OVs are ideal electron-rich centers with abundant confined charges for $O_2$ adsorption, as well as static activation.[22,23] Unfortunately, synthetic defects, especially for OVs, which are typically introduced under harsh conditions (high-temperature annealing, vacuum treatment, or ion sputtering), usually suffer from unavoidable quenching (re-oxidation) along with their interaction with solvent or $O_2$, dictating a decoupling effect.[24,25] Thus, facile engineering generation of OVs to strengthen photon–exciton coupling for charge carrier separation is vital for $O_2$ activation. Besides photon–exciton interaction, another imperative but often neglected aspect of $O_2$ activation is the photoelectron–$O_2$ interaction, as the rate-determining step is associated with the direct interfacial electron-to-$O_2$ transfer. Even $O_2$ can be pre-activated on OVs in many cases; this inherent static interaction cannot ensure dynamic abstraction of electrons upon the excitation of semiconductors due to the weak coupling between charge carriers and $O_2$. In this regard, smart photocatalyst engineering as an attempt to strengthen complex interactions among photons, charge carriers, and $O_2$ is crucial to boosting ROS generation and achieving deep aromatic VOC oxidation.

In this study, we propose another strategy of energetic photocatalytic $O_2$ activation *via* a sophisticated surface hydrogen bond (HB) network constructed with phosphoric acid and a hydroxyl-rich BiOCl(001) surface. BiOCl is a representative ternary semiconductor of low toxicity and high earth abundance that belongs to the family of V–VI–VII oxide materials. The HB network introduced here is proven to have a dual function scheme, not only reinforcing the energy coupling between photons and charge carriers *via* implementing a facile light-switchable OV generation, but also enabling a new coupling between photoelectrons and $O_2$ for energetic interfacial charge transfer. This proof-of-concept strategy with potential for advanced $O_2$ activation is implemented for successful deep oxidation of indoor toluene.

## Experimental section

### Preparation of photocatalysts

BiOCl single-crystalline nanosheets with the (001) surface exposed were prepared through a simple hydrothermal method. In a typical synthesis, 40 ml of an aqueous solution containing three mmol $Bi(NO_3)_3{\cdot}5H_2O$ was added into a 50 mL Teflon-lined stainless autoclave. Then three mmol KCl was added into the above solution under continuous stirring. The autoclave was hydrothermally treated at 160 °C for 12 h. A white precipitate after the hydrothermal reaction was washed with distilled water/ethanol several times, and dried in an oven at 100 °C. BiOCl single-crystalline nanosheets with a (010) surface were prepared through a similar hydrothermal method. The only difference is that after three mmol KCl was added into the $Bi(NO_3)_3{\cdot}5H_2O$ solution, the pH value of the solution was adjusted to about 6.0 using 1 M NaOH. Then, the autoclave was hydrothermally treated at 160 °C for 24 h, and the white precipitate was collected in the same way. For comparison, $BiPO_4$ was prepared through the same hydrothermal method except that an equal molar of $Na_3PO_4{\cdot}12H_2O$ replaced KCl. To prepare phosphoric acid-modified BiOCl (P-BiOCl), we dispersed 0.1 g BiOCl powder in 10 mM phosphoric acid solution under ultrasonication for 5 min. Then the BiOCl and phosphoric acid mixture was placed in the dark with constant stirring for 2.5 h. The as-obtained P-BiOCl precipitate was then washed with distilled water/ethanol and dried in an oven at 100 °C. Phosphoric acid-modified Degussa P25 $TiO_2$ (P-P25) was prepared through the same way except that BiOCl was replaced by an equal weight of P25.

### Theoretical calculations

Theoretical calculations were conducted using the Vienna *Ab initio* Simulation Package (VASP), which utilized the density functional theory (DFT) + *U* and projector augmented-wave

 

(PAW) method.[26,27] Generalized gradient approximation in the scheme of Perdew–Burke–Ernzerhof (GGA-PBE) was adopted to describe the exchange-correlation energy functional.[28]

To optimize the BiOCl(001) surface with and without phosphoric acid adsorption, we first tested the thickness of the atomic layers by applying the (1 × 1) surface to all the models. The plane-wave pseudopotential approach and ultrasoft pseudopotentials were adopted for all the atoms with a kinetic energy cutoff of 380 eV.[29] The structures were relaxed to an energy convergence of $10^{-5}$ eV per atom and force convergence of 0.03 eV $Å^{-1}$. A Monkhorst–Pack mesh BiOCl(001) surface with and without PA adsorption was 3 × 3 × 1. To simulate the $O_2$ activation on surfaces, a (2 × 2) supercell was used and enabled by plane-wave expansion with an energy cutoff of 520 eV. During the $O_2$ adsorption, the energy and force converged to $10^{-5}$ eV per atom and 0.02 eV $Å^{-1}$, respectively. *K*-points for the Brillouin zone were set as 2 × 2 × 1, and the vacuum was kept at 20 Å for all the models. The charge density difference was calculated *via*: $\Delta\rho = \rho(\mathrm{BiOCl} + O_2) - \rho(O_2) - \rho(\mathrm{BiOCl})$. $\rho$(Adsorbate) and $\rho$(BiOCl) are respectively the densities of the two non-interacting subsystems, whereas $\rho(\mathrm{BiOCl} + O_2)$ is the density of the interacting $O_2$–BiOCl system.

### Photocatalytic toluene oxidation

Photocatalytic toluene oxidation is coupled with the filtration technique through immobilizing photocatalysts onto filtration media. BiOCl nanosheets were first deposited onto the glass fiber filter through an aerosol method for the photoreactivity test. A 100 mL suspension of BiOCl nanosheets with a concentration of 2 wt% was sonicated in an ultrasonic bath under ambient conditions. The solution was then connected to an atomizer (Aerosol Generator 3079A, TSI Inc.). Dispersed BiOCl sheets in the form of droplets were directly led to a chamber with a 9.5 mm diameter and finally deposited on a circular glass fiber filter (AX1720HD, LydAir MG ASHRAE, Lydall) with a diameter of 47 mm, a nominal thickness of 0.37 mm and a basis weight of 68 g $m^{-2}$. The filter was kept in place by a stainless steel pressure filter holder (Millipore Corporation) with an effective diameter of 35 mm. Glass fiber media loaded with P-BiOCl nanosheets or $BiPO_4$ were prepared through the same way. Catalytic degradation was performed in a stainless steel reactor of the filter holder type according to our previous work (Fig. S1†).[30] The toluene concentration tested was 10 ppm, and the gas was circulated within the system before the UV lamp (368 nm, 0.6 mW $cm^{-2}$) was turned on. The concentration of toluene throughout the reaction was measured by using a gas chromatograph with a flame ionization detector (GC-FID) that was connected to the reactor. The mineralization efficiency ($M$%) is calculated as $M\% = E(CO_2)/T(CO_2)$, in which $E(CO_2)$ is the experimentally evolved $CO_2$ as measured using a GC-FID and $T(CO_2)$ is the theoretically evolved $CO_2$ assuming toluene is completely mineralized. The $CO_2$ (ppm) was determined by GC-FID equipped with an additional methanizer (methane reforming furnace).

## Results and discussion

The BiOCl(001) surface has a close-packed structure with exposed O atoms (Fig. S2†). During the synthesis, adsorption of protons of high abundance onto the BiOCl(001) surface will enrich the surface with hydroxyl groups (Fig. 1).[31,32] Phosphoric acid is a typical polyprotic acid of both HB-donor and HB-acceptor nature. As expected, without substituting the surface hydroxyl groups, phosphoric acid interacts with the BiOCl(001) surface through HBs (–OH···O), which involves two types of extensive HBs (Fig. 1). Specifically, hydroxyl groups and coordinatively unsaturated O atoms of the BiOCl(001) surface respectively acts as the HB-donor and HB-acceptor to double-bonded O and hydroxyl groups of phosphoric acid (Fig. 2a). Meanwhile, the as-formed HBs are shown to be strong with two typical lengths of 1.75 Å and 1.67 Å, reflecting high stability of the overall structure.[33] Successful elucidation of the specific structures further allowed us to calculate and compare the surface OV formation energy at different atomic locations on the BiOCl(001) surface (Fig. 2b). Within a short-range around the adsorbed phosphoric acid, it is interesting to note that the nearer the surface O atoms to the phosphoric acid, the smaller the OV formation energy (Fig. 2c). Notably, for $O_1$ located at the *ortho* position of phosphoric acid, its OV formation energy was significantly decreased from 3.09 eV to 1.83 eV.

It is widely accepted that OVs serve as ideal electron-rich centers for static $O_2$ binding and activation.[22,23] The decreased formation energy of surface OVs indicates the presence of more reactive sites for $O_2$ activation during photocatalysis, whereas the process of electron transfer from OVs to $O_2$ after phosphoric acid modification is another possible determinant for ROS generation. On OVs of the BiOCl(001) surface, $O_2$ can be adsorbed by forming chemical bonds with two nearest Bi atoms in the sublayer to form a side-on bridging coordination complex (Fig. 2d). According to the magnetic moment (0.79 $\mu_0$) and activated O–O bond length (1.32 Å), $O_2$ on the OVs of the BiOCl(001) surface is shown to be in the superoxide radical ($^{\bullet}O_2^-$) state.[23,34] Interestingly, in the presence of phosphoric acid, the O–O bond of OV-adsorbed $^{\bullet}O_2^-$ is further activated to 1.33 Å (Fig. 2e). Rather than chemically interacting with phosphoric acid, one O atom of $^{\bullet}O_2^-$ shares a subtle and localized HB interaction to the hydroxyl group of PA with a length of 1.80 Å (Fig. 2e). Typically, free $O_2$ will not interact with phosphoric acid *via* HB, and origination of this delicate HB is therefore ascribed to $O_2$ activation. According to the charge density difference, prominent electron depletion around the OVs and subsequent symmetric electron transfer to adsorbed $O_2$ make the adsorbed $^{\bullet}O_2^-$ a credible HB acceptor (Fig. 2d). As reflected by the unsymmetrical isodensity contour plot of the charge density increase at the O atom close to phosphoric acid, the overall electrons populating from OVs to the anti-bonding $2\pi^*$ orbital of the $O_2$ molecule after phosphoric acid adsorption

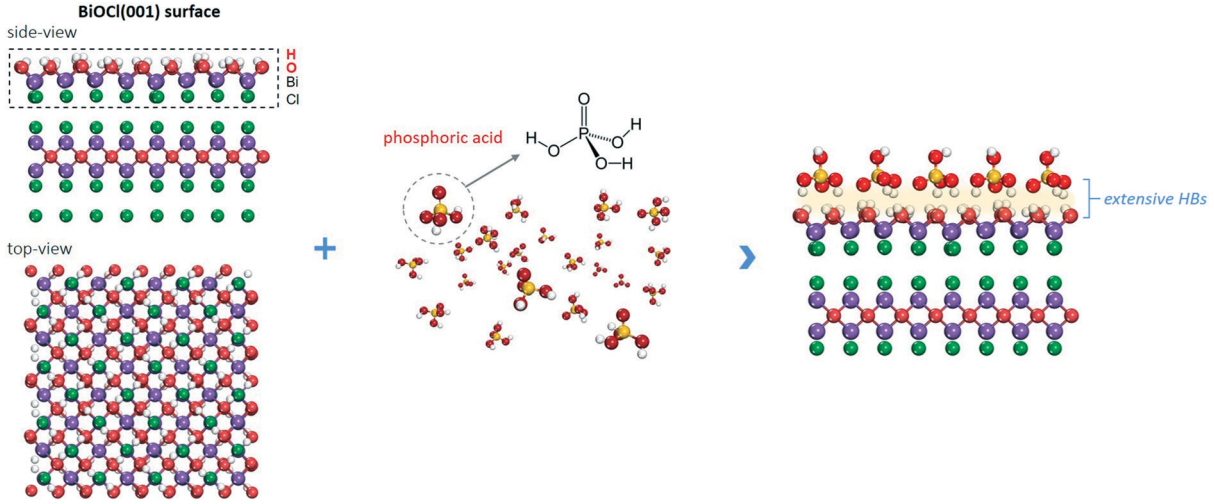


Fig. 1 Schematic illustration of the BiOCl(001) surface and the formation of surface extensive HBs.

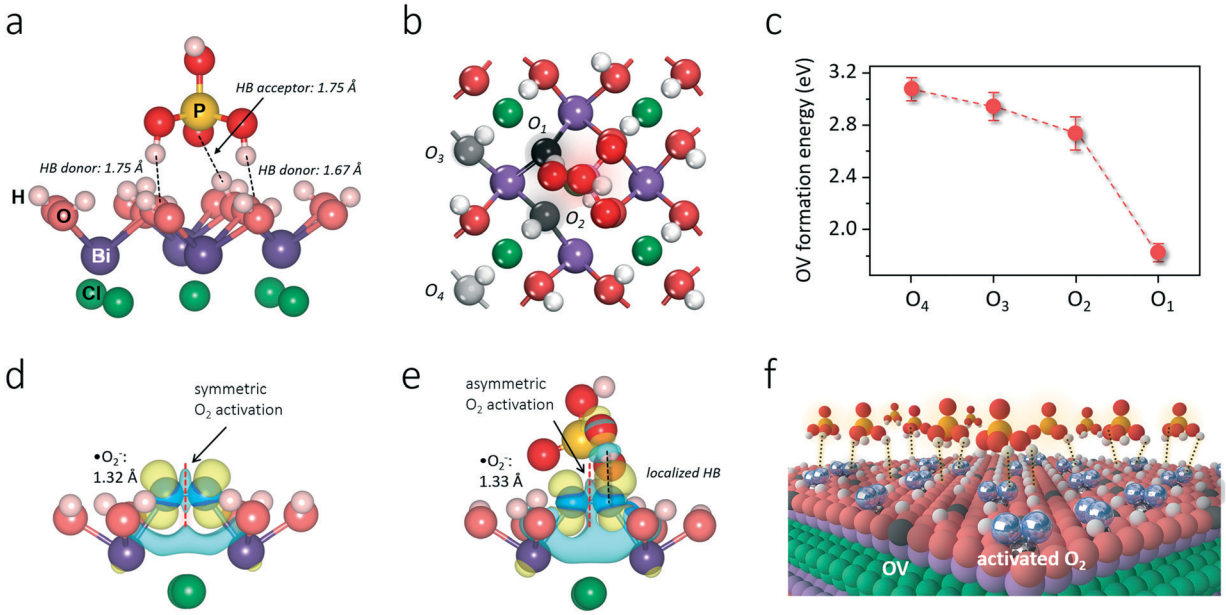


Fig. 2 Influence of HBs on OV formation and $O_2$ activation on the BiOCl(001) surface. (a) Representative HBs on the BiOCl surface with phosphoric acid acting as both the HB donor and acceptor. (b) Top view of the phosphoric acid-adsorbed BiOCl surface and (c) OV formation energies at different locations around phosphoric acid. Charge density difference of the $O_2$-adsorbed BiOCl complex structure with (d) and without phosphoric acid adsorption (e). (f) Schematic illustration of the HB network on OV formation and $O_2$ activation.

are more favorable than those on the clean BiOCl(001) surface (Fig. 2e).

Intuitively, this theoretical scenario presents us a dual-function scheme of the HB network constructed between a hydroxyl-rich BiOCl(001) surface and phosphoric acid, which not only lowers the energy cost towards OV formation but also further promotes interfacial electron transfer towards strong $O_2$ activation (Fig. 2f). To confirm these theoretical predictions, we prepared single-crystalline BiOCl nanosheets with the (001) surface exposed *via* a facile hydrothermal method. Phosphoric acid-modified BiOCl (P-BiOCl) was prepared *via* a simple impregnation method. For comparison, $BiPO_4$ was prepared through a similar hydrothermal process. The scanning electron microscopy (SEM) image shows the smooth surface of BiOCl single-crystalline nanosheets, and corresponding elemental mapping demonstrates the uniform distribution of phosphoric acid (Fig. 3a and S3†). Since no X-ray diffraction (XRD) peaks indexed to $BiPO_4$ were detected for P-BiOCl, the formation of $BiPO_4$ domains on the P-BiOCl surface was thus ruled out (Fig. 3b).

The creation of $BiPO_4$ domains on P-BiOCl was further ruled out through X-ray photoelectron spectroscopy (XPS) analysis. The high-resolution Bi 4f spectrum of BiOCl exhibits two peaks at 165.6 and 160.2 eV, which are characteristic of

 

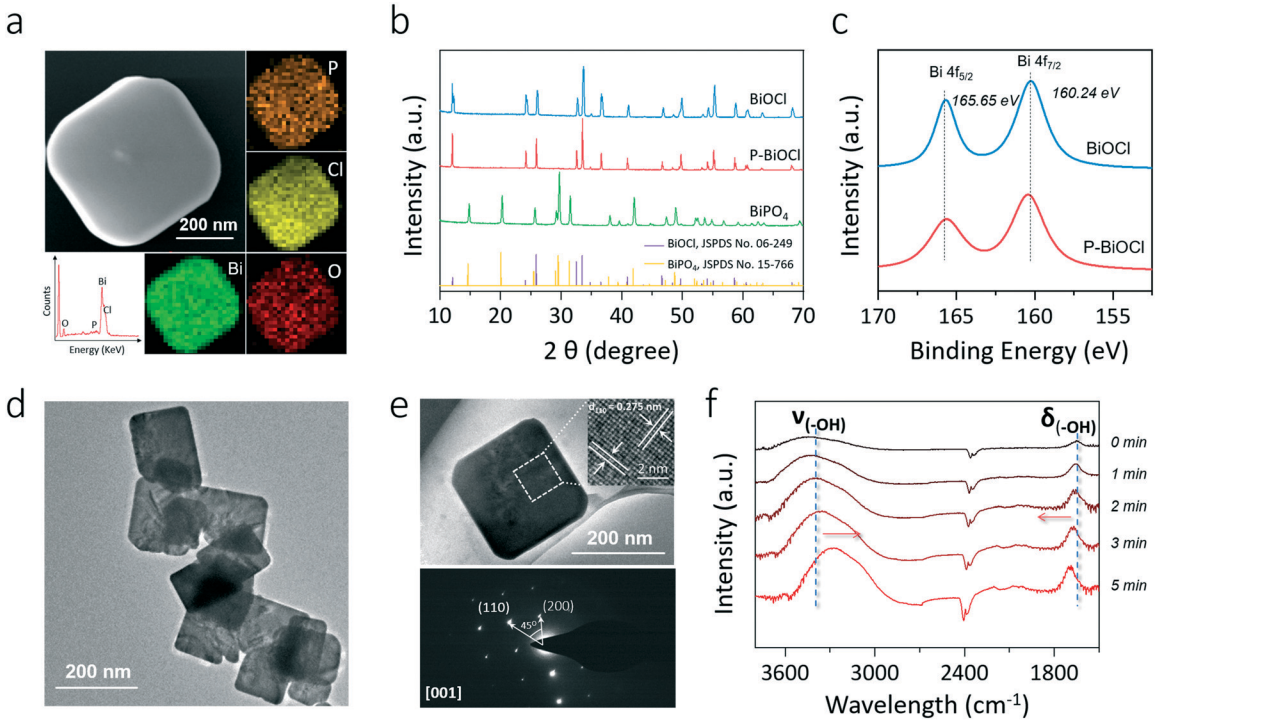


**Fig. 3** Characterization of the as-prepared photocatalysts and surface HBs. (a) SEM-mapping pictures of P-BiOCl surface elements (P, Cl, O, Bi). (b) XRD patterns and (c) XPS spectra of the as-prepared photocatalysts. (d) TEM image of P-BiOCl nanosheets, (e) high-resolution TEM image and SAED pattern of an individual P-BiOCl nanosheet. (f) Temporal evolution of the ATR-FTIR spectra of BiOCl along with phosphoric adsorption.

$Bi^{3+}$ in BiOCl.[35] After phosphoric acid adsorption, Bi 4f XPS binding energies of P-BiOCl experienced no remarkable change (Fig. 3c). Besides XRD and XPS, XPS valence-band (VB) spectra further revealed the electronic structure in terms of the VB position of BiOCl experiencing no remarkable change, suggesting the weak HB interactions between BiOCl and phosphoric acid (Fig. S4†). For comparison, we prepared another typical BiOCl(010) surface.[29] However, due to the coordinating unsaturated Bi atoms on the surface, chemical bonds, rather than hydrogen bonds, were formed after phosphoric acid adsorption (Fig. S5†).

The transmission electron microscopy (TEM) image shows the sheet-shaped morphology of P-BiOCl and the selected area electron diffraction (SAED) pattern of the individual nanosheet indicates the single-crystalline characteristic (Fig. 3d and e). The clear lattice fringes with an interplanar lattice spacing of 0.275 nm correspond to the (110) atomic planes that are perpendicular to the (001) surface of BiOCl. The labeled-angle of 45° agrees well with the theoretical value of the angle between the (110) and (200) planes of BiOCl (Fig. 3e).[36] The set of diffraction spots can be indexed to the [001] zone axis of tetragonal BiOCl, suggesting that the as-prepared P-BiOCl nanosheets are (001)-surface-exposed. To explicitly characterize the possible formation of HB, attenuated total reflectance Fourier transform infrared (ATR-FTIR) spectroscopy was then employed. Along with adsorption of phosphoric acid on the BiOCl surface, the stretching band of –OH of phosphoric acid at 3000–3500 $cm^{-1}$ gradually shifted to a lower wavenumber while the deformation band of –OH around 1700 $cm^{-1}$ shifted to a higher wavenumber, both of which validated the formation of the interfacial HB network (Fig. 3f).[37,38]

To explore whether the formation of the HB network would lower surface OV formation energy, the generation of OVs under light illumination was monitored through *in situ* XPS (Fig. 4a and b). Two additional XPS peaks can reflect surface OVs with lower binding energies at 163.8 and 158.4 eV due to the partial reduction of $Bi^{3+}$ to the lower valence-state of $Bi^{(3-x)+}$ around the OVs (Fig. 4c).[35] The concentration of OVs can then be semi-quantitatively determined by the percentage of $Bi^{(3-x)+}$, similar to the determination of OVs by $Ti^{3+}$ in oxygen-deficient $TiO_2$ (Fig. 4c).[39,40] OV generation is much easier than that on a clean BiOCl surface according to the faster increase of $Bi^{(3-x)+}$ peaks in the Bi 4f XPS spectrum of P-BiOCl (Fig. 4a and b). Temperature-programmed desorption (TPD) was used to detect $O_2$ adsorption on BiOCl and P-BiOCl. As for defect-free BiOCl and P-BiOCl, we did not identify any $O_2$ desorption, suggesting no $O_2$ was adsorbed on their surfaces either physically or chemically (Fig. S6†). This result is consistent with theoretical calculations that $O_2$ interacted weakly with the defect-free BiOCl(001) surface.[34] However, under UV light illumination with the *in situ*-formed OVs, we were able to observe a broad molecular $O_2$ desorption peak from 420 to 650 K on both BiOCl and P-BiOCl, which was related to chemisorbed $O_2$ on photocatalysts bearing OVs. Moreover, oxygen-deficient P-BiOCl displayed a broader and stronger $O_2$ desorption peak located at a higher temperature range than BiOCl, indicating

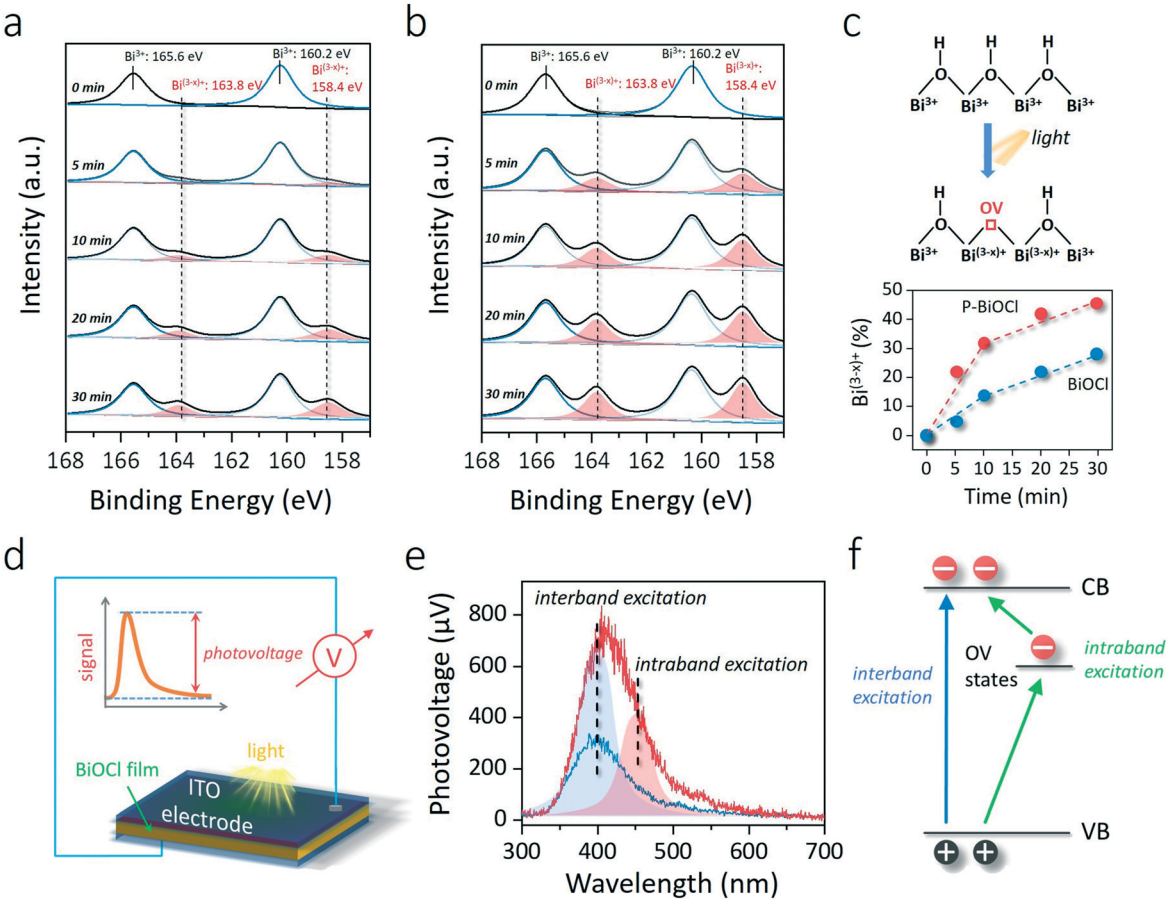


**Fig. 4** Experimental analysis of OV formation and charge separation for BiOCl with and without surface HBs. *In situ* Bi 4f XPS spectra of BiOCl (a) and P-BiOCl (b) under light irradiation. (c) Schematic illustration of the OV formation process and semi-qualitative determination of their concentration change. (d) Schematic of the surface photovoltaic cell that records the change of the catalyst surface photovoltage before and after light irradiation. (e) Steady-state SPV spectra of BiOCl and P-BiOCl and (f) the proposed excitation processes.

a more substantial capacity of P-BiOCl to generate OVs and chemically bind $O_2$. The facile formation of oxygen vacancies was due to rapid transfer and trapping of photoholes by lattice O on the P-BiOCl surface, which was demonstrated by *in situ*-detected $O_2$ released under UV light (Fig. S7†).

As we mentioned above, enhanced OV formation is usually shown to reinforce the interaction between photons and charge carriers for improved separation efficiency. To prove this hypothesis, we adopted steady-state surface photovoltage (SPV) to evaluate the charge carrier separation within the as-prepared photocatalysts. SPV is a contactless and non-destructive technique to probe photophysics within solid-state materials whose signal arises from the change in surface potential barriers before and after light illumination (Fig. 4d).[41–43] Hence, the extent of charge carrier separation can be reflected by the amplitude of the SPV signal. For BiOCl, UV light could excite BiOCl and generate a steady SPV spectrum similar to its UV-vis optical absorption spectra, confirming that charge carrier formation and separation were directly triggered by interband excitation (Fig. 4e and S8†). In comparison with BiOCl, the SPV amplitude of P-BiOCl is first shown to be markedly enhanced, suggesting an improved electron–hole separation efficiency (Fig. 4e). Meanwhile, P-BiOCl displays an additional band-tail excitation up to 600 nm in the visible light region. The tail excitation was fitted with a peak around 453 nm adjacent to the dominant interband excitation peak at 398 nm (Fig. 4e). Since OV-associated defect states usually lie beneath the conduction band (CB) of BiOCl, the SPV emission at longer wavelength was therefore attributed to the indirect excitation of BiOCl.[35,44] During the indirect excitation process, *in situ*-formed OVs acted as the springboard to capture and mediate the transfer of electrons from the VB to CB, thus inhibiting electron–hole recombination (Fig. 4f).

To explore whether facile OV formation and inhibited charge carrier recombination enabled by HBs would positively promote photocatalytic $O_2$ activation, we detected the formation of ROS along with *in situ* OV formation through electron spin resonance (ESR). With 5-*tert*-butoxycarbonyl 5-methyl-1-pyrroline*N*-oxide (BMPO) as a spin-trapping agent in dimethylsulfoxide (DMSO), the superoxide species in the semifree or free state was captured to form a BMPO/$^{\bullet}O_2^-$ adduct having a spectrum with four typical peaks and relative intensities of 1:1:1:1

(Fig. 5a and b).[45] Based on the UV-vis absorption spectra and XPS VB spectra, the electronic energy-level diagram of BiOCl is depicted in Fig. S9,† showing that both the conduction band and oxygen vacancy-associated energy levels are capable of activating $O_2$ to $^{\bullet}O_2^-$. It is to be noted that without changing the valence state of BiOCl, *in situ*-formed OVs would introduce localized vacancy states below the conduction band (Fig. S9a†).[34,44] Plotting the signal intensity against the irradiation time gave a straight line, whose slope directly revealed the generation rate of $^{\bullet}O_2^-$ and was calculated to be 139.5 a.u. $min^{-1}$ for BiOCl and 503.9 a.u. $min^{-1}$ for P-BiOCl (Fig. 5c). The $O_2$ activation rate of P-BiOCl was over 3.6 times that of BiOCl. Intriguingly, OV generation on the P-BiOCl surface was merely 2.2 times that of BiOCl in the beginning (Fig. 4c). In the later stage (after 10 min), the overall OV concentration was only ~1.1 times higher than that of BiOCl (Fig. 4c). In theory, the OV on the BiOCl(001) surface is a single-electron-trapped center, suggesting that for each OV, it will confine the formation of only one molecule of $^{\bullet}O_2^-$ (Fig. 2d). If each $^{\bullet}O_2^-$ adsorbed on OVs is fully activated (into the semi-free or free state) on OVs, an enhanced $^{\bullet}O_2^-$ generation rate of BiOCl after phosphoric adsorption should be identical or close to that of increased OV concentration. It is therefore clear that a considerable amount of $^{\bullet}O_2^-$ remained static and tightly bound to the BiOCl surface, while phosphoric acid with HB interaction to OV-adsorbed $^{\bullet}O_2^-$ obviously helped to free the $^{\bullet}O_2^-$ from OVs through promoting interfacial electron transfer as theoretically predicted above (Fig. 2e and S10†). $^{\bullet}O_2^-$ in different chemical states could be further differentiated through FTIR spectroscopy. The FTIR experiments were carried out through a designed reaction cell in an $O_2$ atmosphere. Under light irradiation, the change of the functional groups on BiOCl surfaces could be monitored *in situ*. On a clean BiOCl surface, a band around 1180 $cm^{-1}$ appeared, being assigned to adsorbed $^{\bullet}O_2^-$ species in a symmetric state (Fig. 5d).[46] As for P-BiOCl, the absorption band ascribed to $^{\bullet}O_2^-$ became more pronounced under light irradiation. Meanwhile, $^{\bullet}O_2^-$ adsorbed on P-BiOCl experienced a redshift to 1145 $cm^{-1}$, which can be explained by the lengthened O–O double bond due to asymmetric activation by the HB (Fig. 2d, e, and 5d).

The subtle HB interaction between the OV-adsorbed $O_2$ and phosphoric acid could be explicitly explored by time-resolved photoluminescence (PL), an informative technique to characterize surface weak interactions based on evolved charge carrier lifetimes.[47,48] The PL decaying curves were collected at the emission peak around 600 nm with atmospheric $O_2$, which was the indirect radiative recombination of electrons on the OVs with photoholes on the VB.[35] We denoted such defect PL emission as $PL_{OV}$. In an $O_2$ atmosphere, decaying $PL_{OV}$ of BiOCl could be fitted using

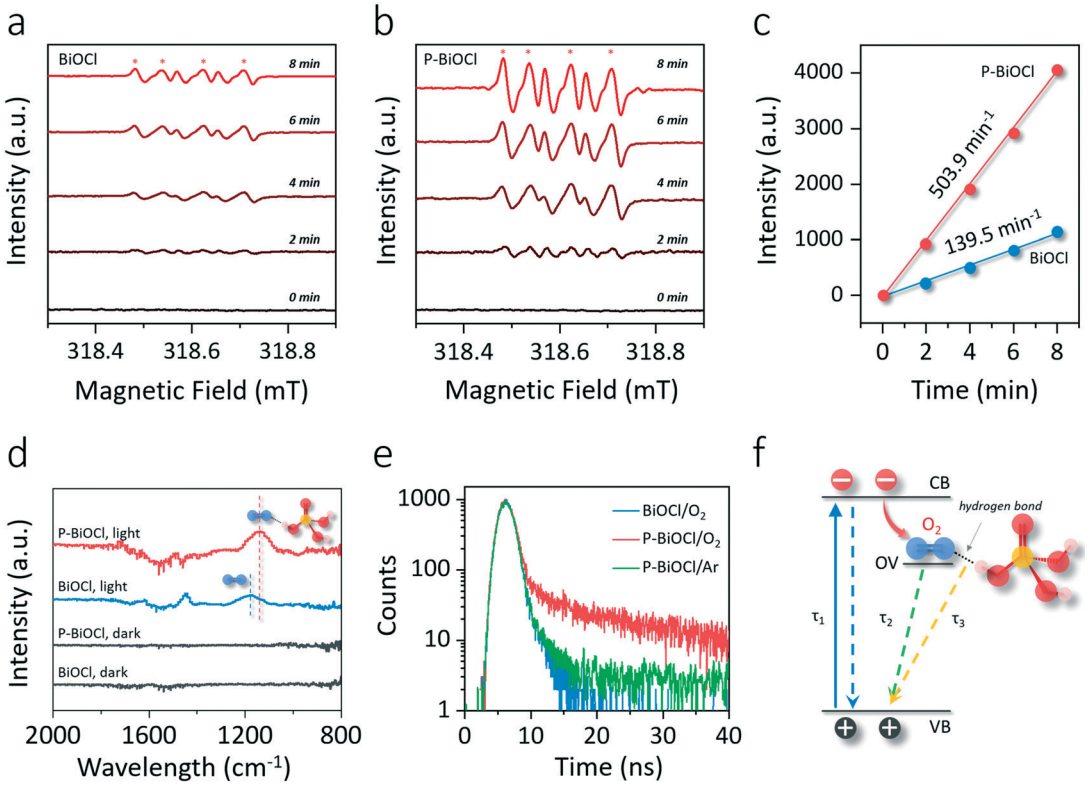


**Fig. 5** Influence of HBs on $O_2$ activation and charge carrier lifetimes of BiOCl. ESR spectra of BiOCl (a) and P-BiOCl (b) towards the generation of $^{\bullet}O_2^-$ under light irradiation. (c) Qualitative determination of $^{\bullet}O_2^-$ generation rate based on the intensity of the ESR-$^{\bullet}O_2^-$ signal. (d) FTIR spectra of BiOCl and P-BiOCl in an $O_2$ atmosphere. (e) Time-resolved PL decay curves of BiOCl and P-BiOCl in different atmospheres. (f) Schematic of recombination processes and corresponding lifetimes of P-BiOCl.

a double-exponential function, including a fast decay component ($\tau_1$) due to interband charge carrier recombination and a much longer lifetime arising from OV-mediated indirect charge carrier recombination (Fig. 5e and Table 1).[35,48] According to the relative contribution of the given lifetimes, the average lifetime for BiOCl ($\tau_{BiOCl}$) was calculated to be 1.08 ns (Table 1). Interestingly, decaying $PL_{OV}$ of P-BiOCl could not be fitted by a double-exponential model, and a third exponential constant ($\tau_3$) around 8.23 ns with a considerable proportion was needed to obtain a better fit, giving a much longer average lifetime ($\tau_{P\text{-}BiOCl}$) of around 3.01 ns (Fig. 5f and Table 1). The lengthened PL lifetime of P-BiOCl in comparison with that of BiOCl was due to the promoted charge carrier separation, agreeing well with SPV results. To trace the origin of $\tau_3$, we then switched the $O_2$ atmosphere to an inert Ar atmosphere and specifically monitored the change of the PL decaying behavior of P-BiOCl (Fig. 5e). Without $O_2$, PL of P-BiOCl displayed a considerably faster decay, and proper fitting could be realized only using the double-exponential model without using $\tau_3$. This fitting led to a remarkably shortened average lifetime ($\tau_{P\text{-}BiOCl/Ar}$) of around 2.24 ns (Table 1). Therefore, $\tau_3$ was directly related to the trapping of photoelectrons by adsorbed $O_2$ on the P-BiOCl surface (Fig. 5f). Since the PL decay curve of BiOCl was not associated with $\tau_3$ even in the $O_2$ atmosphere, it is reasonable to predict that the localized HB interactions facilitated the trapping of photoelectrons by OV-adsorbed $O_2$. Some more specific characterization methods are still needed to verify this hypothesis in the future. This unambiguously unveiled a new photoelectron–$O_2$ interaction mode implemented by HBs, which surmounted the sluggish kinetics of $O_2$ activation.

As we mentioned above, the preparation of photocatalysts with strong $O_2$ adsorption and activation capability is the key to deeply oxidizing aromatic VOCs. In light of this fact, the application of this conceptual $O_2$ activation methodology for indoor toluene removal was simulated through a customized cycling reaction system. After 60 min of light irradiation, BiOCl only removed 55% of toluene, while P-BiOCl was able to eliminate toluene in 30 min (Fig. 6a). For comparison, $BiPO_4$ showed even poorer reactivity for photocatalytic toluene oxidation than BiOCl (Fig. 6a). Meanwhile, the pseudo-first-order kinetic constant of P-BiOCl for toluene oxidation was 11 times higher than that of BiOCl (Fig. 6b). The metal-to-ligand charge transfer mechanism was ruled out according to the O-exposed surface structure and UV-vis absorption spectra of P-BiOCl after the adsorption of toluene (Fig. S11a and b†). 10 mM phosphoric acid was found to be the optimum concentration to functionalize BiOCl (Fig. S11c†). Even phosphoric acid modification would lead to negative charge accumulation on the BiOCl surface and the possible formation of a surface electrostatic field, such an effect was not the dominant factor for the observed significant photoreactivity increase of BiOCl (Fig. S12†).[49–52] These results reveal that adsorbed phosphoric acid dramatically enhanced the photocatalytic removal efficiency of BiOCl for toluene oxidation through HB interactions. Besides toluene removal efficiency, another critical concern is mineralization efficiency. As we mentioned above, incomplete oxidation of toluene would result in the accumulation of carbonaceous intermediates, thus deactivating the photocatalysts. The mineralization efficiency was determined through total organic carbon (TOC) measurements based on evolved $CO_2$ and theoretical TOC. Although BiOCl removed 55% of toluene in 60 min, the mineralization efficiency was less than 30%, while P-BiOCl was able to completely oxidize 83% of toluene to $CO_2$ and $H_2O$ (Fig. 6c). For repeated cycles of toluene oxidation, BiOCl displayed a gradual photoreactivity decrease due to the accumulation of abundant carbonaceous intermediates (Fig. 6d). The carbonaceous intermediates were more strongly adsorbed on the surface than the parent toluene molecule, directly causing catalyst deactivation. P-BiOCl displayed much better photoreactivity than commercial Degussa P25 mixed-phase $TiO_2$ with and without phosphoric acid modification, as well as good photostability for five cycles of toluene oxidation (Fig. 6d and S13†). The high stability of P-BiOCl was not only due to *in situ*-OV generation but also the facile OV regeneration for long term $O_2$ activation based on the color change of the OV-associated color-center (Fig. S14†). For the photocatalyst composed of physically mixed BiOCl and phosphoric acid, its photoreactivity was much weaker than that of P-BiOCl (Fig. S15a†). Meanwhile, P-BiOCl maintained its phase structure for sustainable toluene

**Table 1** Parameters of the time-resolved PL decay curves

| Photocatalyst | Decay time (ns) | | | Relative percentage (%) | | | Average lifetime[a] (ns) | $R^2$ |
|---|---|---|---|---|---|---|---|---|
| | $\tau_1$ | $\tau_2$ | $\tau_3$ | $I_1$ | $I_2$ | $I_3$ | | |
| $BiOCl/O_2$ | 0.85 | 4.68 | — | 94 | 6 | — | 1.08 | 0.98 |
| $P\text{-}BiOCl/O_2$ | 0.78 | 4.36 | 8.23 | 55 | 29 | 16 | 3.01 | 0.96 |
| P-BiOCl/Ar | 0.82 | 4.2 | — | 58 | 42 | — | 2.24 | 0.92 |

[a] The decaying curve can be fitted using a multiexponential function $I_{PL}(t) = \sum_{i=1}^{n} A_i e^{t/\tau_i}$, where $I_{PL}(t)$ represents the PL intensity, $\tau_i$ the decay time, and $A_i$ the amplitude. Average lifetime $<\tau>$ is calculated by $\langle\tau\rangle = \sum_{i=1}^{n} c_i\tau_i$, where $c_i$ is the relative concentration in the multiexponential decay and is expressed as $c_i = A_n / \sum_{i=1}^{n} A_i$.

 

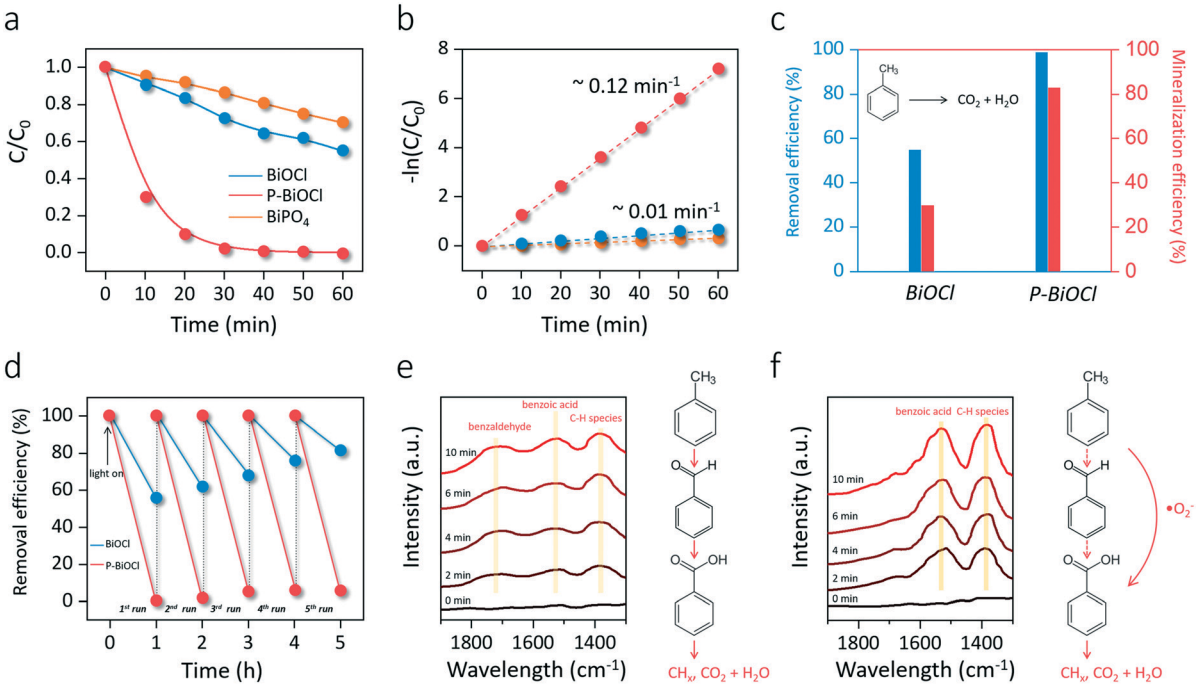


**Fig. 6** Photoreactivity and stability of the as-prepared photocatalysts for simulated toluene oxidation and the detected intermediates. (a) Photocatalytic toluene oxidation and (b) the corresponding pseudo-first-order rate constants. (c) Mineralization efficiency of toluene in comparison with the removal efficiency over BiOCl and P-BiOCl. (d) Multicycle toluene oxidation with BiOCl and P-BiOCl. *In situ* FTIR spectra with intermediate species evolution during photocatalytic toluene oxidation on BiOCl (e) and P-BiOCl (f). Proposed toluene oxidation pathways are shown in (e) and (f), in which the red lines represent the sequential oxidation and blue lines the ring cleavage towards mineralization. Dotted lines indicate the inhibited pathways.

removal, and adsorption of phosphoric acid experienced no remarkable loss (Fig. S15b and c†). It is believed the deactivation of P-BiOCl was avoided due to a sufficient supply of ROS and the efficient mineralization of toluene. Broadly conceived, the formation of carbonaceous intermediates that caused catalyst deactivation is directly caused by the sluggish aromatic ring-opening process, an essential prerequisite for deep oxidation. To experimentally probe the aromatic ring-opening process, *in situ* FTIR was first adopted to dynamically monitor the temporal evolution of some key surface intermediates during photocatalytic toluene oxidation. After the adsorption equilibrium of toluene was achieved, characteristic absorption bands indexed to the toluene (2855 $cm^{-1}$) and aromatic ring (2884 $cm^{-1}$) could be observed on both BiOCl and P-BiOCl (Fig. S16†).[53] After the light was turned on, absorption bands corresponding to toluene on the BiOCl surface gradually decreased, while new typical bands corresponding to intermediates of benzaldehyde (1712 $cm^{-1}$) and benzoic acid (1528 $cm^{-1}$) gradually increased (Fig. 6e).[53–55] Meanwhile, a prominent peak indexed to the C–H vibration of hydrocarbon species ($CH_x$) emerged, which were the critical intermediates along with aromatic ring-opening (Fig. 6e).[47,50] These results suggested that toluene was sequentially oxidized to benzaldehyde and benzoic acid. Benzoic acid would be further decomposed into benzene through the photo-Kolbe (decarboxylation) reaction ($C_6H_5$–COOH → $C_6H_6$ + $CO_2$).[14] Both benzoic acid and benzene are easier to cleave than toluene or benzaldehyde, generating intermediate $CH_x$ species towards mineralization.[12] As for P-BiOCl, it is interesting to note that formation of benzaldehyde was not detected, while accumulation of benzoic acid and $CH_x$ species became more pronounced than those on the BiOCl surface (Fig. 6f). Meanwhile, toluene removal on P-BiOCl is also more environmentally friendly as benzaldehydes with a lower oxidation degree, but higher toxicity was restrained, while benzoic acid with lower toxicity was preferentially generated.[56]

Gas chromatography–mass spectrometry (GC–MS) and liquid chromatography–mass spectrometry (LC–MS) were further adopted to verify the intermediates associated with photocatalytic toluene oxidation. First, it is worth noting that no gaseous intermediates were detected by on-line GC-FID in our case, which is in agreement with previous studies. Some researchers proposed that only when the photocatalysts were heated would gaseous intermediates be released. To this end, we tried to extract the intermediates on the BiOCl and P-BiOCl surface. To collect as many intermediates as possible, we increased the initial concentration of toluene to 50 ppm. Methanol was used to extract surface intermediates under ultrasonication. After the centrifugation, the supernatant was collected and concentrated through rotary evaporation and nitrogen blowing. Then, the condensed solution was directly analyzed through GC–MS and LC–MS.

Among the abundant organic species, benzaldehyde, benzoic acid, benzyl alcohol were the three critical intermediates on the BiOCl and P-BiOCl surface. At the same time, no mono-hydroxylated isomers were detected, including hydroxybenzaldehyde, hydroxybenzoic acid, and hydroxybenzyl alcohol. These mono-hydroxylated isomers were often found during $TiO_2$-mediated toluene oxidation (Table S1†). It is known that methyl group hydrogen and aromatic ring hydrogen are the two kinds of hydrogen atoms in toluene (Fig. S17†).[14,56,57] The first pathway (I) of photocatalytic toluene oxidation has been confirmed as the abstraction of hydrogen from the methyl group to generate benzyl radicals, which is considered the rate-determining step (Fig. S17†).[58] Through this pathway, benzyl radicals can be further oxidized into the three critical intermediates in the early stage, *i.e.* benzaldehyde, benzoic acid and benzyl alcohol. Besides, the aromatic ring of toluene can also be hydroxylated by $^{\bullet}OH$ through the second pathway (II) (Fig. S17†).[59,60] The absence of mono-hydroxylated isomers indicated that attack of $^{\bullet}OH$ on the aromatic ring was not a significant pathway in our photocatalytic system. Since the concentration of $^{\bullet}OH$ is closely related to oxidation of water by photoholes ($H_2O + h^+ \rightarrow {}^{\bullet}OH + H^+$), Sleiman *et al.* suggested that the second pathway was only promoted at a very high relative humidity level by the increase in the population of $^{\bullet}OH$.[14]

Since it is challenging to quantify the exact concentrations of the above three critical intermediates on BiOCl and P-BiOCl surfaces, we indirectly compared the relative amounts of the intermediates based on their abundance in the mass spectra. Interestingly, the concentrations of benzaldehyde and benzyl alcohol were much higher on the BiOCl surface than those on the P-BiOCl surface in the primary stage, while more benzoic acid was accumulated on the P-BiOCl surface (Table S2†). Usually, the dominant reactive species responsible for the sequential photocatalytic oxidation of toluene to benzaldehyde and benzoic acid are considered as photoholes and $^{\bullet}OH$.[61,62] In a typical process, benzyl radicals can be formed by hole oxidation with fast proton release or direct hydrogen abstraction by $^{\bullet}OH$. The surface benzyl radical can then react with $O_2$ to form a benzylperoxy radical, which will be coupled to form a tetroxide species.[59,63] The tetroxide decomposes to benzaldehyde, benzyl alcohol, and $O_2$ through the Russell reaction.[64] Benzaldehyde oxidizes quickly into benzoic acid in the presence of $O_2$.[65,66] To explore the influence of holes on toluene oxidation, sodium oxalate ($Na_2C_2O_4$) was mixed with BiOCl for toluene oxidation (Fig. S18a†). As compared with toluene, $Na_2C_2O_4$ is much more easily oxidized and mineralized by photoholes, thus it can serve as the hole scavenger.[67] The overall inhibition efficiency for photocatalytic toluene removal was estimated to be 49% and 30% for BiOCl and P-BiOCl, respectively, suggesting that photoholes of BiOCl played a more important role in toluene oxidation than those of P-BiOCl. Notably, we only detected a 20% decrease of the surface benzoic acid on P-BiOCl (Table S2†), suggesting that besides photoholes and $^{\bullet}OH$, other essential species actively participated in photocatalytic toluene oxidation on the P-BiOCl surface. When *p*-benzoquinone was added to quench the surface $^{\bullet}O_2^-$ of P-BiOCl, photocatalytic toluene oxidation was largely inhibited (Fig. S18b and c†). The addition of *tert*-butyl alcohol (TBA) and catalase respectively as the $^{\bullet}OH$ and $H_2O_2$ scavenger did not remarkably influence the photoreactivity of BiOCl or P-BiOCl for toluene oxidation (Fig. S18d–f†). Thus, $^{\bullet}OH$ and $H_2O_2$ were not the primary reactive species of BiOCl and P-BiOCl, possibly due to low humidity during toluene oxidation in the gas phase. It is, therefore, reasonable to propose that $^{\bullet}O_2^-$ also actively participated in the critical kinetic step associated with oxidation of toluene into benzaldehyde and benzoic acid on the P-BiOCl surface. This hypothesis was evidenced by previous studies that either benzyl radicals or benzylperoxy radicals could be directly oxidized by $^{\bullet}O_2^-$ to benzaldehyde.[59,60,65,68,69] As long as toluene was oxidized to benzaldehyde, subsequent oxidation of benzaldehyde to benzoic acid could easily proceed in the presence of reactive molecular oxygen species. As expected, when benzaldehyde was used as the target pollutant, the photocatalytic conversion efficiency of benzaldehyde on P-BiOCl was over two times that of BiOCl (Fig. S19†). The temporal change in the concentrations of benzaldehyde, benzyl alcohol, and benzoic acid on BiOCl and P-BiOCl surfaces also supported the hypothesis that the rapid generation of $^{\bullet}O_2^-$ by P-BiOCl accelerated the catalytic oxidation of toluene into benzoic acid *via* benzaldehyde (Fig. S20†). These results are consistent with the *in situ* FTIR spectra that toluene was more rapidly oxidized to benzoic acid on the P-BiOCl surface. Thus, the generation of more $^{\bullet}O_2^-$ by P-BiOCl would cooperate with photoholes and accelerate the kinetic step associated with toluene oxidation to benzoic acid *via* benzaldehyde in the primary stage.

Besides benzaldehyde, benzoic acid, and benzyl alcohol, other typical intermediates were detected, including benzene, succinic acid, pyruvic acid, propionic acid, and acetic acid, all of which were associated with the aromatic ring opening towards deep oxidation. Based on the above intermediates and analysis, we propose a possible photocatalytic toluene oxidation pathway in our photocatalytic system (Fig. 7). Upon UV light irradiation, toluene is oxidized to benzyl radicals by photoholes or $^{\bullet}OH$, which is usually the rate-determining step for its oxidation. Typically, a surface benzyl radical can reache tetroxide decomposes to benzaldehyde, benzyl alcohol, and $O_2$ through the Russell reaction. The presence of $^{\bullet}O_2^-$ apparently accelerates this process by directly oxidizing benzyl radicals or benzylperoxy radicals to benzaldehyde. Because of the rapid conversion of benzaldehyde to benzoic acid by $^{\bullet}O_2^-$, less benzaldehyde was accumulated on the P-BiOCl surface. After benzaldehyde was efficiently oxidized to benzoic acid with the help of $^{\bullet}O_2^-$, the aromatic ring of benzoic acid would be easily cleaved, or, benzoic acid can undergo a photo-Kolbe (decarboxylation) reaction to give benzene and $CO_2$.[14,56] Short-chain alcoholic, aldehydic and

 

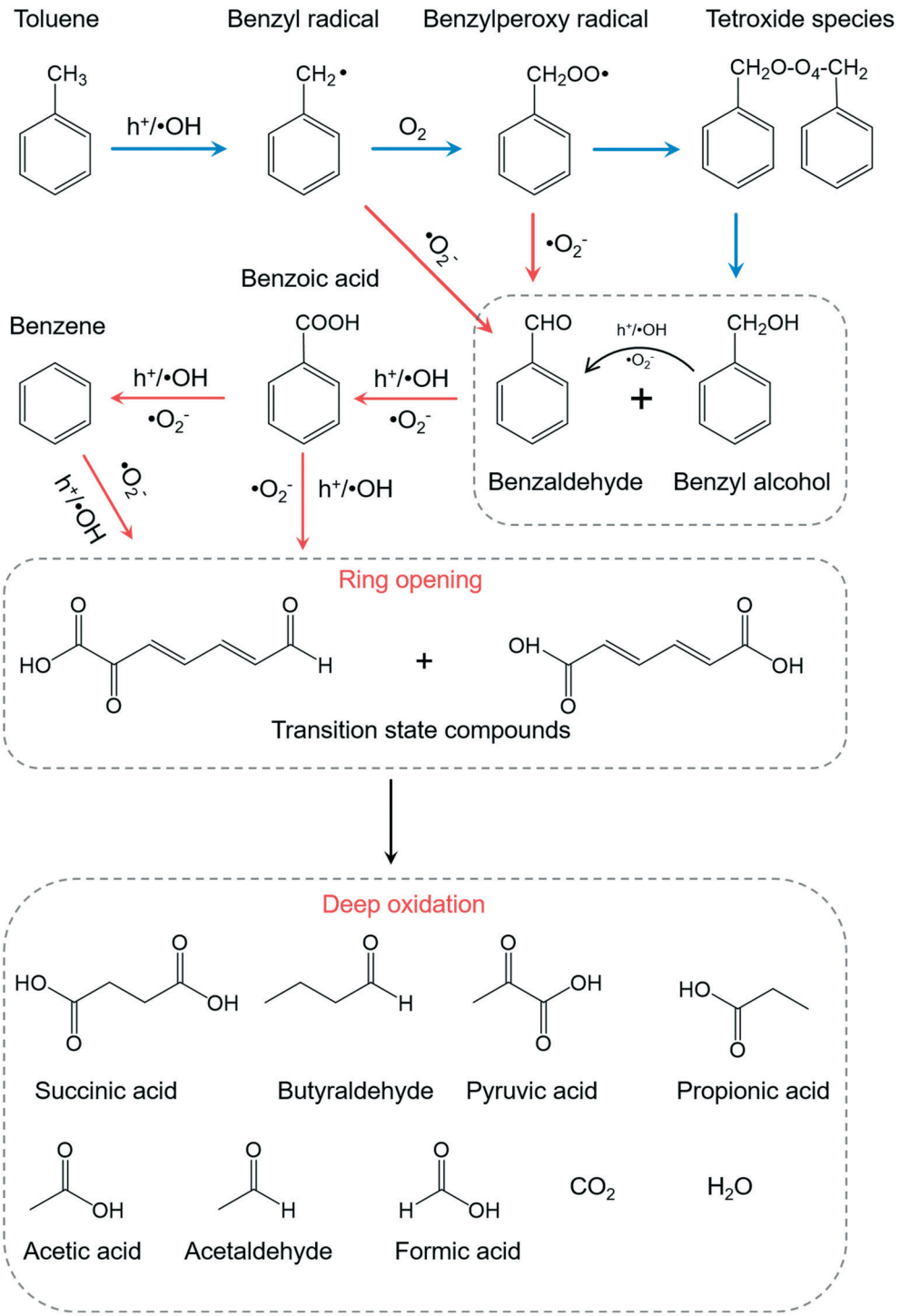


**Fig. 7** Proposed reaction pathways for the photocatalytic toluene oxidation.

acidic intermediates will be formed after the benzene ring opening. Further bond breakage of these intermediates by reactive species ($h^+$, $^{\bullet}OH$, $^{\bullet}O_2^-$) produces much smaller molecular products corresponding to deep toluene oxidation products, including propionic acid, acetic acid, formic acid, acetaldehyde, $CO_2$, and $H_2O$. Thus, the enhanced formation of $^{\bullet}O_2^-$ accelerated the kinetic processes associated with the primary oxidation of toluene into benzaldehyde and benzoic acid, as well as aromatic ring opening towards deep oxidation. This was the very reason why the lower concentrations of stubborn intermediates and higher mineralization degree are achieved on P-BiOCl, both of which will ensure the excellent stability and sustainability of photocatalysts for VOC removal. Meanwhile, the facile synthesis of BiOCl photocatalysts on a gram scale allows us to prepare a novel functional filter, which can be scaled up and installed on a commercial air cleaner for practical application.[70,71]

## Conclusions

State-of-the-art indoor air VOC removal based on adsorption technology possesses certain drawbacks, including poor capability for dilute VOCs, low-efficiency under relatively high humidity, risky adsorbent desorption, and limited regeneration ability. Photocatalytic VOC removal under ambient conditions is thus encouraging to tackle these challenges through harvesting of light energy and green $O_2$. Although considerable efforts have been devoted to developing various photocatalysts for VOC removal, low-efficiency and poor recyclability of these photocatalysts due to insufficient supply of ROS restrict their practical application. The sophisticated surface HB network introduced in this study is shown to exhibit a dual function. The extensive HBs established between the hydroxyl-rich BiOCl surface and phosphoric acid are first shown to weaken surface Bi–O bonds, enabling facile OV generation significantly. OVs act as reliable centers for electron capture and static $O_2$ activation, reinforcing the interaction between photons and excitons for rapid charge carrier separation. Moreover, dynamic $O_2$ activation with sluggish kinetics can be surmounted by another type of HB localized between hydroxyl groups of phosphoric acid and OV-adsorbed $O_2$. These unique localized HBs facilitate interfacial electron transfer from BiOCl to $O_2$, displaying a unique energy coupling route between charge carriers and reactants. For simulated indoor toluene oxidation, the substantially boosted $O_2$ activation is shown to accelerate the kinetic processes associated with the primary oxidation of toluene into benzaldehyde and benzoic acid, as well as aromatic ring opening towards deep oxidation. Undesirable intermediate accumulation and catalyst deactivation are thus avoided. The present work highlights the pivotal roles of HBs in robust photocatalytic $O_2$ activation. It will provide novel insights into the design of high-performance catalysts for efficient and safe control of indoor VOCs.

## Conflicts of interest

There are no conflicts to declare.

## Acknowledgements

This work was partially supported by the Center for Filtration Research (CFR) at the University of Minnesota. We thank Dr. Artur Braun for providing GC system for part of our photocatalytic toluene removal experiments.

## Notes and references

1 A. Cincinelli and T. T. Martellini, *Int. J. Environ. Res. Public Health*, 2017, **14**, 1286.
2 P. Fantke, L. Huang, M. Overcash, E. Griffing and O. Jolliet, *Green Chem.*, 2020, **22**, 6008–6024.
3 S. Brosillon, M.-H. Manero and J.-N. Foussard, *Environ. Sci. Technol.*, 2001, **35**, 3571–3575.
4 F. Haghighat, C.-S. Lee, B. Pant, G. Bolourani, N. Lakdawala and A. Bastani, *Atmos. Environ.*, 2008, **42**, 8176–8184.
5 I. I. Laskar, Z. Hashisho, J. H. Phillips, J. E. Anderson and M. Nichols, *Environ. Sci. Technol.*, 2019, **53**, 2647–2659.
6 L. I. Granone, F. Sieland, N. Zheng, R. Dillert and D. W. Bahnemann, *Green Chem.*, 2018, **20**, 1169–1192.
7 C. Li, Y. Xu, W. Tu, G. Chen and R. Xu, *Green Chem.*, 2017, **19**, 882–899.
8 H. Li, J. Li, Z. Ai, F. Jia and L. Zhang, *Angew. Chem., Int. Ed.*, 2018, **57**, 122–138.
9 C. Mao, J. Wang, Y. Zou, H. Li, G. Zhan, J. Li, J. Zhao and L. Zhang, *Green Chem.*, 2019, **21**, 2852–2867.
10 I. Salem, N. Keller and V. Keller, *Green Chem.*, 2009, **11**, 966.
11 S. Weon, E. Choi, H. Kim, J. Y. Kim, H.-J. Park, S. Kim, W. Kim and W. Choi, *Environ. Sci. Technol.*, 2018, **52**, 9330–9340.
12 J. Li, X. Dong, G. Zhang, W. Cui, W. Cen, Z. Wu, S. C. Lee and F. Dong, *J. Mater. Chem. A*, 2019, **7**, 3366–3374.
13 H. Li, Z. Ai and L. Zhang, *Chem. Commun.*, DOI: 10.1039/D0CC05449F.
14 M. Sleiman, P. Conchon, C. Ferronato and J.-M. Chovelon, *Appl. Catal., B*, 2009, **86**, 159–165.
15 L. Cao, Z. Gao, S. L. Suib, T. N. Obee, S. O. Hay and J. D. Freihaut, *J. Catal.*, 2000, **196**, 253–261.
16 L. Sun, G. Li, S. Wan and T. An, *Chemosphere*, 2010, **78**, 313–318.
17 F. Zhang, M. Wang, X. Zhu, B. Hong, W. Wang, Z. Qi, W. Xie, J. Ding, J. Bao, S. Sun and C. Gao, *Appl. Catal., B*, 2015, **170–171**, 215–224.
18 Y.-Z. Ma, L. Valkunas, S. L. Dexheimer, S. M. Bachilo and G. R. Fleming, *Phys. Rev. Lett.*, 2005, **94**, 157402.
19 E. Hendry, J. M. Schins, L. P. Candeias, L. D. A. Siebbeles and M. Bonn, *Phys. Rev. Lett.*, 2004, **92**, 196601.
20 H. Wang, X. Sun, D. Li, X. Zhang, S. Chen, W. Shao, Y. Tian and Y. Xie, *J. Am. Chem. Soc.*, 2017, **139**, 2468–2473.
21 H. Wang, D. Yong, S. Chen, S. Jiang, X. Zhang, W. Shao, Q. Zhang, W. Yan, B. Pan and Y. Xie, *J. Am. Chem. Soc.*, 2018, **140**, 1760–1766.
22 Y.-F. Li, U. Aschauer, J. Chen and A. Selloni, *Acc. Chem. Res.*, 2014, **47**, 3361–3368.
23 U. Aschauer, J. Chen and A. Selloni, *Phys. Chem. Chem. Phys.*, 2010, **12**, 12956–12960.
24 M. Xing, J. Zhang, F. Chen and B. Tian, *Chem. Commun.*, 2011, **47**, 4947.
25 S. Wang, X. Hai, X. Ding, K. Chang, Y. Xiang, X. Meng, Z. Yang, H. Chen and J. Ye, *Adv. Mater.*, 2017, **29**, 1701774.
26 G. Kresse and J. Furthmüller, *Comput. Mater. Sci.*, 1996, **6**, 15–50.
27 G. Kresse and D. Joubert, *Phys. Rev. B: Condens. Matter Mater. Phys.*, 1999, **59**, 1758–1775.
28 J. P. Perdew, K. Burke and M. Ernzerhof, *Phys. Rev. Lett.*, 1996, **77**, 3865–3868.
29 D. Vanderbilt, *Phys. Rev. B: Condens. Matter Mater. Phys.*, 1990, **41**, 7892–7895.
30 F. Denny, E. Permana, J. Scott, J. Wang, D. Y. H. Pui and R. Amal, *Environ. Sci. Technol.*, 2010, **44**, 5558–5563.
31 J. Jiang, K. Zhao, X. Xiao and L. Zhang, *J. Am. Chem. Soc.*, 2012, **134**, 4473–4476.

 

32 X. Liu, H. Yang, H. Dai, X. Mao and Z. Liang, *Green Chem.*, 2015, **17**, 199–203.
33 H. Li, J. Shang, H. Zhu, Z. Yang, Z. Ai and L. Zhang, *ACS Catal.*, 2016, **6**, 8276–8285.
34 K. Zhao, L. Zhang, J. Wang, Q. Li, W. He and J. J. Yin, *J. Am. Chem. Soc.*, 2013, **135**, 15750–15753.
35 H. Li, H. Shang, Y. Li, X. Cao, Z. Yang, Z. Ai and L. Zhang, *Environ. Sci. Technol.*, 2019, **53**, 6964–6971.
36 J. Jiang, K. Zhao, X. Xiao and L. Zhang, *J. Am. Chem. Soc.*, 2012, **134**, 4473–4476.
37 L. Kőrösi, S. Papp, S. Beke, A. Oszkó and I. Dékány, *Microporous Mesoporous Mater.*, 2010, **134**, 79–86.
38 H. Sheng, H. Zhang, W. Song, H. Ji, W. Ma, C. Chen and J. Zhao, *Angew. Chem., Int. Ed.*, 2015, **54**, 5905–5909.
39 B. Bharti, S. Kumar, H.-N. Lee and R. Kumar, *Sci. Rep.*, 2016, **6**, 32355.
40 C. Jin, B. Liu, Z. Lei and J. Sun, *Nanoscale Res. Lett.*, 2015, **10**, 95.
41 L. Kronik, *Surf. Sci. Rep.*, 1999, **37**, 1–206.
42 L. Kronik and Y. Shapira, *Surf. Interface Anal.*, 2001, **31**, 954–965.
43 H. Li, F. Qin, Z. Yang, X. Cui, J. Wang and L. Zhang, *J. Am. Chem. Soc.*, 2017, **139**, 3513–3521.
44 H. Li, J. Shi, K. Zhao and L. Zhang, *Nanoscale*, 2014, **6**, 14168–14173.
45 M. Xu, Y. Chen, J. Qin, Y. Feng, W. Li, W. Chen, J. Zhu, H. Li and Z. Bian, *Environ. Sci. Technol.*, 2018, **52**, 13879–13886.
46 L. Vaska, *Acc. Chem. Res.*, 1976, **9**, 175–183.
47 Z. Bian, T. Tachikawa, P. Zhang, M. Fujitsuka and T. Majima, *Nat. Commun.*, 2014, **5**, 3038.
48 H. Li, J. Shang, Z. Ai and L. Zhang, *J. Am. Chem. Soc.*, 2015, **137**, 6393–6399.
49 D. Zhao, C. Chen, Y. Wang, H. Ji, W. Ma, L. Zang and J. Zhao, *J. Phys. Chem. C*, 2008, **112**, 5993–6001.
50 F. Chen, J. Zhao and H. Hidaka, *Res. Chem. Intermed.*, 2003, **29**, 733–748.
51 M. Xie, J. Bian, M. Humayun, Y. Qu, Y. Feng and L. Jing, *Chem. Commun.*, 2015, **51**, 2821–2823.
52 Z. Wang, A. Mahmood, X. Xie, X. Wang, H. Qiu and J. Sun, *Chem. Eng. J.*, 2020, **393**, 124723.
53 S. Besselmann, E. Löffler and M. Muhler, *J. Mol. Catal. A: Chem.*, 2000, **162**, 401–411.
54 J. Li, H. Na, X. Zeng, T. Zhu and Z. Liu, *Appl. Surf. Sci.*, 2014, **311**, 690–696.
55 Y. Irokawa, T. Morikawa, K. Aoki, S. Kosaka, T. Ohwaki and Y. Taga, *Phys. Chem. Chem. Phys.*, 2006, **8**, 1116.
56 W. Zhao, J. Dai, F. Liu, J. Bao, Y. Wang, Y. Yang, Y. Yang and D. Zhao, *Sci. Total Environ.*, 2012, **438**, 201–209.
57 J. Mo, Y. Zhang, Q. Xu, Y. Zhu, J. J. Lamson and R. Zhao, *Appl. Catal., B*, 2009, **89**, 570–576.
58 S. Andersson, *J. Catal.*, 1986, **98**, 138–149.
59 O. d'Hennezel, P. Pichat and D. F. Ollis, *J. Photochem. Photobiol., A*, 1998, **118**, 197–204.
60 *Physico-Chemical Behaviour of Atmospheric Pollutants*, ed. G. Restelli and G. Angeletti, Springer Netherlands, Dordrecht, 1990.
61 H. Huang and W. Li, *Appl. Catal., B*, 2011, **102**, 449–453.
62 L. Bo, S. Xie, H. Meng, J. Liu and B. Gao, *Catal. Lett.*, 2017, **147**, 1623–1630.
63 C. von Sonntag and H.-P. Schuchmann, *Angew. Chem., Int. Ed. Engl.*, 1991, **30**, 1229–1253.
64 G. A. Russell, *J. Am. Chem. Soc.*, 1957, **79**, 3871–3877.
65 M. Wang, J. Hua and Y. Yang, *Spectrochim. Acta, Part A*, 2018, **199**, 102–109.
66 F. Zhang, X. Zhu, J. Ding, Z. Qi, M. Wang, S. Sun, J. Bao and C. Gao, *Catal. Lett.*, 2014, **144**, 995–1000.
67 J. Jiang, L. Zhang, H. Li, W. He and J. J. Yin, *Nanoscale*, 2013, **5**, 10573.
68 P. O'Neill, *Int. J. Radiat. Biol. Relat. Stud. Phys., Chem. Med.*, 1987, **52**, 976.
69 M. Fujihira, Y. Satoh and T. Osa, *Bull. Chem. Soc. Jpn.*, 1982, **55**, 666–671.
70 C. H. Ao and S. C. Lee, *Chem. Eng. Sci.*, 2005, **60**, 103–109.
71 S. Weon and W. Choi, *Environ. Sci. Technol.*, 2016, **50**, 2556–2563.